

Strength of single-crystal orthopyroxene under lithospheric conditions

Tomohiro Ohuchi · Shun-ichiro Karato ·
Kiyoshi Fujino

Received: 22 February 2010 / Accepted: 13 August 2010 / Published online: 2 September 2010
© Springer-Verlag 2010

Abstract Creep strength of oriented orthopyroxene single crystals was investigated via shear deformation experiments under lithospheric conditions [P (pressure) = 1.3 GPa and T (temperature) = 973–1,373 K]. For the A-orientation (shear direction [001] on (100) plane), the samples have transformed completely to clinoenstatite and much of the deformation occurred after transformation. In contrast, for the B-orientation (shear direction [001] on (010) plane), samples remained orthoenstatite and deformation occurred through dislocation motion in orthoenstatite. The strength of orthopyroxene with these orientations is smaller than for olivine aggregates under all experimental conditions. Flow of the B-orientation samples is described by a power-law, and the pre-exponential constant, the apparent activation energy, and the stress exponent are determined to be $A = 10^{-9.5} \text{ s}^{-1} \cdot \text{MPa}^{-4.2}$, $Q = 114 \text{ kJ/mol}$ and $n = 4.2$. However, for the A-orientation, the results cannot be fit by a single flow law and we obtained the following: $A = 10^{8.9} \text{ s}^{-1} \cdot \text{MPa}^{-3.0}$, $Q = 459 \text{ kJ/mol}$ and $n = 3.0$ at high temperatures ($\geq 1,173 \text{ K}$), and $A = 10^{-27.4} \text{ s}^{-1} \cdot \text{MPa}^{-14.3}$, $Q = 296 \text{ kJ/mol}$ and $n = 14.3$ at low temperatures ($< 1,173 \text{ K}$). The stress exponent for the low-temperature regime is high, suggesting that deformation involves some processes where the activation energy decreases with stress such as the Peierls mechanism.

Our study shows that orthopyroxene with these orientations is significantly weaker than olivine under the lithospheric conditions suggesting that orthopyroxene may reduce the strength of the lithosphere, although the extent to which orthopyroxene weakens the lithosphere depends on its orientation and connectivity.

Keywords Orthopyroxene · Orthoenstatite · Clinoenstatite · Olivine · Lithosphere

Introduction

The strength of the lithosphere is one of the most important factors that control the style of convection in a planet. The plate tectonic style of convection occurs only when the lithosphere is relatively weak ($< 150 \text{ MPa}$, if a single “strength” is used to characterize the lithosphere deformation) (e.g., Solomatov and Moresi 1997; Tackley 2000; Richards et al. 2001). However, previous models based on olivine rheology predict a higher average strength of the oceanic lithosphere on Earth (a peak stress of $\sim 800 \text{ MPa}$ or higher: Kohlstedt et al. 1995) exceeding the critical strength for plate tectonics. Based on the experimentally obtained creep strength of olivine at relatively low temperatures ($T = 1,173\text{--}1,473 \text{ K}$), Demouchy et al. (2009) pointed out that the published high-temperature power-law creep for olivine overestimates the strength of olivine under the lithospheric conditions, implying that the strength envelopes for the lithosphere calculated by Kohlstedt et al. (1995) overestimate the strength of the lithosphere. Various models have been proposed to reduce the strength of the lithosphere including models based on the weakened shear zones caused by grain-size reduction (e.g., Braun et al. 1999) and frictional heating (Balachandrar

Communicated by H. Keppler.

T. Ohuchi · S. Karato
Department of Geology and Geophysics,
Yale University, New Haven, CT 06520, USA

T. Ohuchi (✉) · K. Fujino
Geodynamics Research Center, Ehime University,
Matsuyama 790-8577, Japan
e-mail: ohuchi@sci.ehime-u.ac.jp

et al. 1995), the “damage” model (Bercovici 2003), and the thermal cracking model (Korenaga 2007). However, these models contain a number of presumptions that are not readily tested against observations (either experimental or geological). Here, we show results of experimental studies showing that a previously ignored mineral, orthopyroxene, might have the key to understanding the strength of the lithosphere.

Because olivine is a volumetrically dominant mineral in Earth and most of other terrestrial planets, the creep strength of olivine has been used in estimating the strength of the lithosphere (Kohlstedt et al. 1995). However, if there is another mineral that has significantly smaller strength but enough volume, then the strength estimate ignoring that phase will be grossly in error. An important secondary phase in the lithosphere is orthopyroxene that occupies ~20–40 volume % of the lithosphere (Carter 1970). Previous studies showed that the creep strength of orthopyroxene is controlled by slip (dislocation creep) or a deformation-induced phase transformation from orthoenstatite to clinoenstatite, and the strength of orthopyroxene could be much smaller than that of olivine under some conditions (Raleigh et al. 1971). However, in these experiments, the stress magnitude was determined by an external load-cell in a Griggs-type apparatus with talc as the confining medium, and these experiments had large uncertainties because of the friction between the piston and the confining medium (Gleason and Tullis 1993). In several studies, the creep strength of the enstatite or enstatite-olivine mixture was studied using a high-resolution gas-medium apparatus at low pressure and high-temperature conditions (Mackwell 1991; Hitchings et al. 1989). However, the stable phase of enstatite is proto-enstatite and not ortho-enstatite under these conditions (Anastasiou and Seifert 1972), and consequently these results cannot be applied to the upper mantle. Orthopyroxene is stable at low pressure and low temperatures (Anastasiou and Seifert 1972), but at these conditions, the creep strength would exceed the confining pressure and one cannot investigate the ductile rheology if one uses a gas-medium deformation apparatus. Therefore, we conclude that there have been no experimental studies on the deformation of orthopyroxene with sufficiently small errors that can be applied to the deformation of Earth’s upper mantle.

In contrast to the direct effects of orthopyroxene suggested by these earlier studies, Warren and Hirth (2006) suggested an indirect influence of orthopyroxene to assist strain localization. These authors argued that orthopyroxene might assist shear localization caused by grain-size reduction of olivine through its influence on retarding grain growth of olivine by the pinning effect. In fact, recent experiments on grain growth in forsterite–pyroxene two-phase systems (Ohuchi and Nakamura 2007; Hiraga et al.

2010) suggest that the grain growth of olivine is strongly prohibited by pyroxene grains. In order for this mechanism to work, fine grains of orthopyroxene must be produced at these lithospheric conditions. However, processes of grain-size refinement of orthopyroxene are unknown. Boullier and Gueguen (1975) (see also Skemer and Karato 2008) suggested an important role of orthopyroxene in the deformation of sheared lherzolites. However, fine-grained orthopyroxene bands seen in sheared lherzolites are not commonly seen in other peridotites and it is not obvious if such a process is important with regard to the deformation of the lithosphere in general.

As a first step to evaluating the role of orthopyroxene on the deformation of the lithosphere, we have conducted a series of experimental studies in which the strength of orthopyroxene single crystals was determined at relatively low-temperature and high-pressure conditions using the Griggs apparatus with an improved method of stress measurement. We report the results of these studies and discuss some of the implications of the present results on the deformation of the lithosphere.

Experimental procedure

Starting materials and sample preparation

The starting materials are gem-quality single crystals of orthopyroxene [approximately $(Mg_{0.91}Fe_{0.09})SiO_3$] from Kilosa, Tanzania. The composition was determined using a JEOL JXA-8600 electron probe microprobe analyzer and is shown in Table 1. Inclusion- and crack-free crystals of orthopyroxene were carefully selected. The crystals were oriented using electron back-scattered diffraction and then core-drilled with a diameter of 2 mm. The core-drilled samples were sectioned at 45° to have a thickness of 400–530 μm and desired orientations which allow the activation of the shear deformation along the [001] direction on either (100) or (010) plane of orthopyroxene. We call the orientation of the former sample type the “A-orientation” and the latter “B-orientation”. The starting materials for olivine aggregates were prepared from a sample of San Carlos olivine ($Fe_{0.0}$). Inclusion-free crystals of olivine were carefully selected and crushed using an agate mortar. The fine-grained powders of olivine stored at 383 K in a vacuum oven were placed into a nickel capsule and were annealed at 1.0 GPa and 1,473 K for ~6 h. The average grain size of the hot-pressed samples measured by the intercept method was obtained to be ~15 μm. The water content of all the samples was measured both before and after deformation experiments using the FT-IR spectroscopy. The methods and results of water content measurements will be described later in this paper.

Table 1 Chemical composition of orthopyroxene

Wt% oxides	
SiO ₂	58.0
TiO ₂	0.1
Al ₂ O ₃	0.2
FeO ^a	6.1
MnO	0.3
MgO	35.0
CaO	0.2
Na ₂ O	0.1
K ₂ O	0.0
Total	100.0
Cations per 6 oxygen	
Si	2.00
Ti	0.00
Al	0.01
Fe	0.18
Mn	0.01
Mg	1.80
Ca	0.01
Na	0.00
K	0.00
Xen	0.91
Xfs	0.09

^a Total Fe calculated as FeO

^b Composition was determined at 15 kV accelerating voltage and 15 nA probe current

Deformation experiments

Shear deformation experiments were conducted using a Griggs apparatus at a constant pressure of $P = 1.3$ GPa, temperature $T = 973$ – $1,373$ K, and shear strain rates of 10^{-3} – 10^{-5} s⁻¹ under water-poor conditions (Table 2). To minimize the friction, we used cesium chloride as a pressure medium surrounding the piston/sample (see Fig. 1). The entire assembly was stored at 383 K for ~12 h in a vacuum oven before each experiment. Uncertainty of the confining pressure resulting from the friction between the cell assembly and pressure vessel is less than 15% (e.g., Mirwald et al. 1975; Rybacki et al. 1998). A sectioned sample of orthopyroxene was placed into a nickel capsule and then sandwiched between alumina pistons (Fig. 1). The water content of each sample was measured after every experiment (Tables 2). The shear direction was [001] and the shear plane was either (100) (for the A-orientation) or (010) (for the B-orientation). In a few runs (GA233 and 235), orthopyroxene was deformed together with a polycrystalline olivine.

Pressure was first raised to the desired value in ~2 h, and then temperature was increased at a rate of ~25 K/min. Temperature was monitored by two Pt/Rh thermocouples

placed close to the upper and lower parts of the sample. The temperature variation between the two thermocouples was usually less than 30 K. After the temperature was stabilized, a piston was advanced at a constant rate. Shear strain was measured by the rotation of a platinum strain-marker, which was initially placed perpendicularly to the shear direction. The uncertainty in the strain rate was usually 10–15%. Samples also underwent shortening. The shortening strain was 9–29%. Because of shortening of the alumina pistons during the deformation experiments, the shear strain measured from the strain-marker rotation was smaller than the shear strain calculated from the displacement of a piston (former ones were 43–100% of latter ones).

The differential stress on the sample was measured with an external load-cell in the Griggs apparatus. Although the use of soft materials such as cesium chloride for the confining medium reduces the friction between the piston and the confining medium (Zhang and Green 2007), friction is still involved in the measured stress. We made a correction for the friction from the load–displacement relation assuming that a “hit point” represents a point at which the load record starts to include the load supported by a sample in addition to the “friction” and that the load caused by friction increases linearly with displacement. A typical example of the load–displacement curve is shown in Fig. 2 indicating a well-defined hit point. We also made the correction for the load supported by a nickel capsule based on the creep data for nickel (Frost and Ashby 1982). This correction was less than 5% of the load supported by a sample.

Even though the use of a soft pressure medium reduces the uncertainties in the stress measurements, this method still has some uncertainties. Consequently, we also used the dislocation-density piezometer for the measurement of stress in some experiments. We used the dislocation density of olivine to infer the stress magnitude using an SEM technique where the total length of dislocation lines per unit volume is measured (Jung and Karato 2001; Karato and Jung 2003). The dislocation density was measured in each olivine polycrystalline sample after oxidation at 1,173 K for 1 h. The oxidized dislocations were observed using the back-scattered electron (BSE) images via a FEG ESEM XL30 scanning electron microscope (SEM) at Yale University. We measured the total length of dislocations per unit volume from the BSE images by calculating the effective thickness from which the BSEs were generated (Karato and Lee 1999). Digitized 8-bit BSE images acquired at magnifications of about 14,000× were converted to binary form leaving the dislocations by using Scion Image© software. The binary images of dislocations were corrected and improved further by using image processing tools available in Adobe Photoshop© and

Table 2 Experimental conditions and results

Run no.	<i>P</i> (GPa)	<i>T</i> (K)	Shear strain (γ) ^a	Shear strain rate (s ⁻¹)	Stress ($\sigma_1 - \sigma_3$) (MPa) ^b	Compressional strain (%)	Initial water content (ppm H/Si) ^c	Water content (ppm H/Si) ^d
A-orientation samples								
GA227	1.3	1,273	1.9 (± 0.3)	2.2 (± 0.3) 10^{-4}	250	10	264 (± 28)	775 (± 99)
GA228	1.3	1,073	1.2 (± 0.2)	1.6 (± 0.2) 10^{-4}	936	10	264 (± 28)	725 (± 128)
GA229	1.3	1,173	1.3 (± 0.2)	1.5 (± 0.2) 10^{-4}	823	26	264 (± 28)	635 (± 72)
GA230	1.3	1,233	1.5 (± 0.2)	1.6 (± 0.2) 10^{-4}	362	23	315 (± 29)	776 (± 54)
GA231	1.3	1,273	1.5 (± 0.2)	4.4 (± 0.7) 10^{-4}	312	22	253 (± 11)	566 (± 63)
GA232	1.3	1,073	1.5 (± 0.2)	3.2 (± 0.5) 10^{-4}	951	24	315 (± 29)	683 (± 107)
GA233	1.3	1,273	2.4 (± 0.4)	1.4 (± 0.2) 10^{-4}	212	22	315 (± 29)	844 (± 136)
GA233 (olivine)			~ 0			9	57 (± 16)	66 (± 13)
GA234	1.3	973	1.2 (± 0.2)	1.7 (± 0.3) 10^{-4}	1,268	10	269 (± 16)	506 (± 121)
GA235	1.3	1,073	1.0 (± 0.1)	2.8 (± 0.4) 10^{-5}	808	29	315 (± 29)	771 (± 37)
GA235 (olivine)			0.4 (± 0.1)			10	57 (± 16)	76 (± 13)
B-orientation samples								
GA217	1.3	1,173	1.0 (± 0.1)	1.2 (± 0.2) 10^{-4}	775	19	340 (± 11)	694 (± 124)
GA218	1.3	1,273	1.1 (± 0.2)	4.1 (± 0.6) 10^{-5}	420	14	250 (± 7)	414 (± 78)
GA219	1.3	1,273	0.8 (± 0.1)	1.3 (± 0.2) 10^{-4}	590	20	340 (± 11)	382 (± 57)
GA220	1.3	1,373	1.1 (± 0.2)	1.4 (± 0.2) 10^{-4}	518	28	340 (± 11)	518 (± 86)
GA221	1.3	1,073	0.9 (± 0.1)	1.3 (± 0.2) 10^{-4}	1,121 ^e	18	250 (± 7)	581 (± 71)
GA222	1.3	1,273	0.7 (± 0.1)	9.2 (± 1.4) 10^{-4}	890	20	327 (± 24)	454 (± 76)
GA224	1.3	1,273	0.8 (± 0.1)	3.1 (± 0.5) 10^{-4}	697	26	327 (± 24)	787 (± 58)
GA225	1.3	1,173	1.1 (± 0.2)	2.4 (± 0.4) 10^{-4}	919	11	292 (± 69)	450 (± 92)

^a Shear strain was measured from the rotation of strain-marker. The uncertainty of the shear strain was estimated from the shape of the strain-marker

^b Stress at the midpoints of steady-state creep for the B-orientation samples and estimated values of the steady-state creep strength for the A-orientation samples

^c Water content in the samples before deformation. The IR spectra were taken along the [010] and [100] direction for the A- and B-orientation samples, respectively

^d Water content in the deformed samples. The IR spectra were taken along the [010] and [100] direction for the A- and B-orientation samples, respectively

^e Stress at the maximum strain (non-steady-state creep strength)

then again converted to binary images. The dislocation outlines were then reduced to a constant thickness of one pixel using a skeletonization function in the image processing software (e.g., Scion Image©). The total length of these skeletonized lines was measured, and then the total length of dislocations per unit volume was calculated. An average value for the dislocation density obtained from the measurement of ~ 40 grains in each sample was used to infer the stress magnitude. The uncertainties of the stress estimation are about ± 10 – 15% from the calibrations and the heterogeneity of the dislocations in a sample (Jung and Karato 2001). This method of dislocation-density measurement is different from a common technique of dislocation-density measurements where the total number of dislocations crossing a given plane is measured (e.g., Kohlstedt et al. 1980), which has a large uncertainty caused by the unknown orientations of dislocation lines.

The relationship between applied stress and dislocation density can be described empirically as follows:

$$\rho = \beta \cdot \sigma^m \quad (1)$$

where ρ is density of free dislocations; β and m , constants; and σ , differential stress ($= \sigma_1 - \sigma_3$) (Kohlstedt et al. 1976). We recalibrated the relationship between σ and ρ of the olivine polycrystalline samples by measuring dislocation density in some samples deformed at known stress levels by Karato et al. (1986), using our newly developed image processing technique for the olivine dislocation-density measurements.

The results are summarized in Table 3. The differential stress obtained by the load-cell is plotted against average dislocation density in olivine samples in Fig. 3a. The steady-state creep strength obtained by an external load-cell in a Griggs apparatus is also plotted. From the stress–dislocation density relation in olivine samples which were

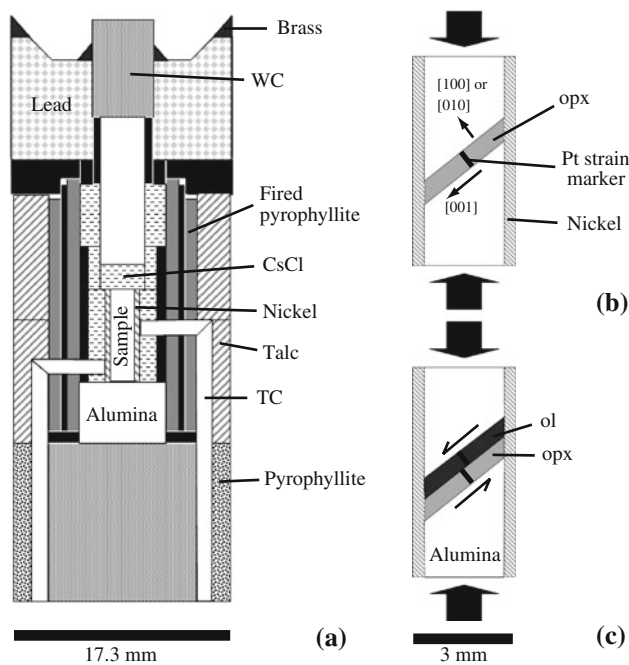


Fig. 1 **a** An experimental assembly viewed in cross section. **b** Sample assemblies with a simple shear design for deformation of orthopyroxene (opx) single-crystal samples and **c** orthopyroxene–olivine (ol) two-layer samples are also shown. Cesium chloride (CsCl) sleeves surround the upper alumina piston and a nickel capsule. Graphite parts are shown in black in Fig. 1a. Large arrows in **b**, **c** represent direction of the axial differential stress ($\sigma_1 - \sigma_3$). Small arrows in **b**, **c** represent the orientation of an orthopyroxene single-crystal sample and the direction of shear stress, respectively. WC: tungsten carbide; TC: Pt/Rh thermocouple in alumina tubes

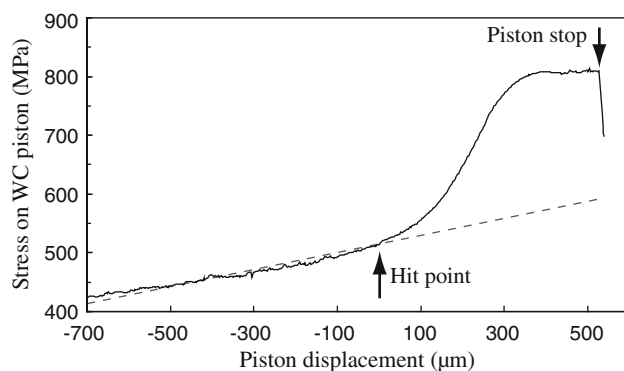


Fig. 2 An example of the relation between stress on the upper tungsten carbide (WC) piston and piston displacement during an experiment (GA219). The upper piston was advanced without deformation of the sample in order to estimate the dependency of stress magnitude of friction on piston displacement. The sample deformation is expected to be started at the point of rapid increase in stress (hit point). We assumed that the stress magnitude of friction linearly increases with piston displacement after the hit point. The expected dependency of friction on piston displacement is shown by the dashed line

deformed using a gas apparatus (Karato et al. 1986), we determined the parameters in Eq. 1 for the olivine polycrystalline: $\log_{10} \beta = 9.21 \pm 0.16$ and $m = 1.39 \pm 0.07$

for σ in MPa and ρ in m^{-2} . Substituting these parameters and values of average dislocation density into Eq. 1, we estimated the differential stress on the olivine samples which were deformed using a Griggs apparatus. The differential stress obtained by the external load-cell is plotted against that by the dislocation-density piezometer in Fig. 3b. Figure 3b shows that the difference in the estimated stress level between the external load-cell and the dislocation-density piezometer is less than 7%. This shows that the differential stress was obtained by the external load-cell within an error of $\sim 10\%$ in this study.

Water content

The water concentration in the samples was measured by Fourier-transform infrared (FTIR) spectroscopy using a mercury cadmium telluride detector with 4 cm^{-1} resolution. The IR spectra were taken from single crystals of orthopyroxene with an unpolarized IR beam incident along the [010] or [100] direction. Spectra were also taken from the polycrystalline olivine samples, which showed absorption bands due to OH-related species in the lattice as well as on grain-boundaries. All the measurements were carried out in air while placing the doubly polished sections of the samples on a KBr plate using a Varian 600 UMA Fourier-transform infrared spectrometer at Yale University. The aperture size of $100 \times 100 \mu\text{m}^2$ was used in all measurements. Infrared spectra were taken at 5 points in each sample. The calibration by Paterson (1982) was used to calculate the amount of water from the IR beam absorption in the range of wave number $3,000\text{--}3,750 \text{ cm}^{-1}$. Measured water contents in the samples are summarized in Table 2. The water content in the orthopyroxene samples before and after deformation is in the range of 250–844 ppm H/Si, showing that the samples are relatively “dry” compared to natural orthopyroxenes in upper mantle xenoliths (e.g., Ingrin and Skogby 2000). Water content in the olivine samples before and after deformation is 57 and 66–76 ppm H/Si, respectively.

Microstructural observations

Microstructures of deformed samples were investigated by using both optical and transmission electron microscopes. Large-scale (the orders of 0.1–1 mm) deformation microstructures were examined using a transmitted polarized-light microscope. A JEOL JEM-2010 transmission electron microscope (TEM) at Ehime University was also used at 200 kV accelerating voltage to investigate the smaller microstructures in deformed samples. Thin specimens for TEM observations were prepared from thin sections which were parallel to the shear direction and perpendicular to the shear plane, and then ion-milled with an accelerating voltage of 3 kV and at an angle of $12\text{--}15^\circ$.

Table 3 Experimental conditions and results for the stress estimation using the olivine dislocation-density piezometer

Run No.	P (GPa)	T (K)	Strain rate (s^{-1}) ^a	$(\sigma_1 - \sigma_3)_{load-cell}$ (MPa) ^b	Dislocation density ($10^{12} m^{-2}$) ^c	$(\sigma_1 - \sigma_3)$ dislocation (MPa) ^d
Samples from Karato et al. (1986) ^e						
4678	0.3	1,573	3.5×10^{-5}	112	1.18 (± 0.18)	–
4721	0.3	1,573	1.1×10^{-4}	262	3.64 (± 0.55)	–
4778	0.3	1,573	1.1×10^{-5}	120	1.16 (± 0.17)	–
4885	0.3	1,573	3.5×10^{-4}	150	1.74 (± 0.26)	–
4920	0.3	1,573	1.2×10^{-5}	130	1.38 (± 0.21)	–
This study ^f						
GA210 ^g	1.0	1,173	5.0×10^{-5}	273	4.08 (± 0.61)	282 (± 31)
GA214 ^g	1.0	1,073	2.0×10^{-5}	521	9.11 (± 1.37)	501 (± 55)
GA233	1.3	1,273	1.4×10^{-4}	151 ^h	1.72 (± 0.26)	152 (± 17)

^a Uniaxial strain rate: Karato et al. (1986), GA210, GA214. Shear strain rate: GA233

^b Differential stress at steady-state creep measured by using a load-cell

^c Average dislocation density in deformed olivine aggregates

^d Differential stress estimated by using the olivine dislocation-density piezometer

^e Deformation experiments were conducted using a gas-medium apparatus

^f Deformation experiments were conducted using a Griggs apparatus

^h Stress at the maximum strain

^g Two-layered samples (orthopyroxene single crystal and olivine aggregate samples were sandwiched together between alumina pistons) were used for the deformation experiments

^h Stress at the maximum strain

Results

Mechanical data

All the stress–strain curves of the samples are shown in Fig. 4. Steady-state creep tends to be achieved by deformation at relatively high temperatures ($T \geq 1,173$ K), but at low temperatures steady-state was not always observed. For example, extensive transient creep behavior was observed for the A-orientation samples (i.e., samples deformed in the A-orientation geometry). In these cases, we estimated the steady-state flow law based on the following procedure. The stress–strain curves for these samples can be divided into three regimes similar to those observed in some metals (Fig. 5): (1) initial period where $d\tau/d\gamma$ is small, (2) intermediate regime where nearly linear strain-hardening is observed, and (3) the later stage of hardening where parabolic hardening is observed. These three stages are observed in some metals and a microscopic model for these stages was proposed (e.g., Seeger 1957). In this model, the stress–strain curves in the later stage [regime (3)] contain information about steady-state creep. Steady-state creep strength was estimated by applying the following formula for the stress–strain curves in this regime using the non-linear least-square fitting method:

$$\tau_\gamma = \tau_s [1 - \exp(-C\gamma)] \quad (2)$$

where τ_γ is the shear stress ($= \sigma_\gamma/2$) at a shear strain γ ; τ_s is the steady-state creep strength ($= \sigma_s/2$); and C is a constant (Smith and Carpenter 1987). The best-fit curves defined as Eq. 2 are shown in Fig. 5. The obtained values of τ_s and C are summarized in Table 4. The C for the A-orientation samples was obtained to be 1.2–4.0, being in the range of reported values for olivine, garnet, and lherzolite ($C = 1.0 \times 10^{-3}$ –250: Smith and Carpenter 1987). Because steady-state creep was approached in most of the deformation of the B-orientation samples (except for GA221), such a correction was not applied with these samples.

The steady-state creep strength is plotted against inverse temperature in Fig. 6. Strain rate is plotted against the steady-state creep strength in Fig. 7. The logarithmic values of stress linearly increase with increasing inverse temperature at a constant strain rate, and increase with increasing strain rate at a constant temperature. The temperature dependence of stress in the deformation of the A-orientation samples drastically changes at $\sim 1,200$ K, suggesting a change in deformation mechanism. This is consistent with the result that the strain-rate dependence of creep strength of the A-orientation samples at 1,073 K is quite different from that at 1,273 K. Figure 8 shows the backscattered electron images of orthopyroxene deformed together with

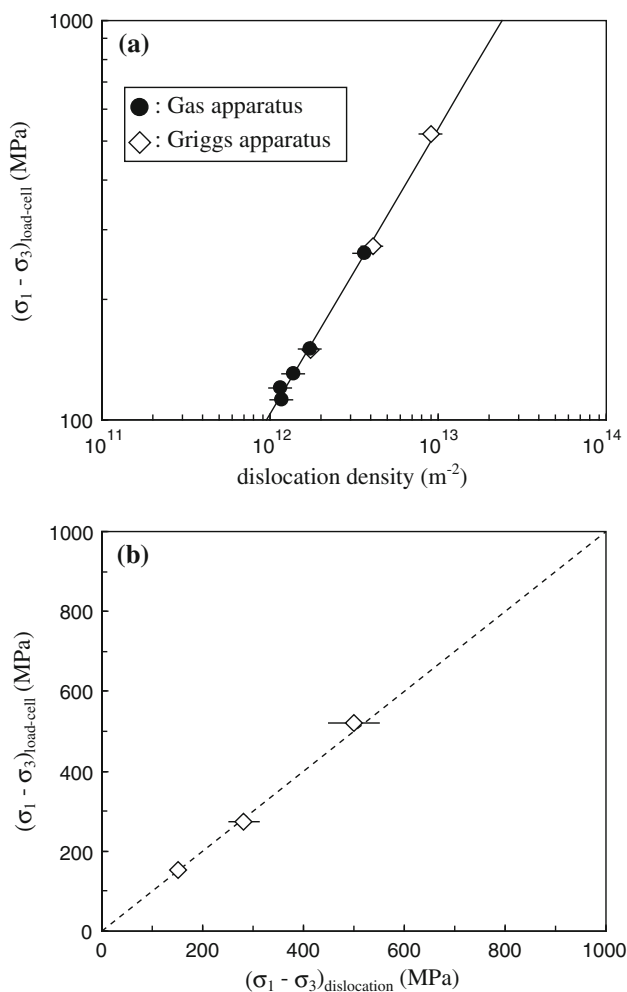


Fig. 3 **a** Differential stress on the steady-state creep measured by a load-cell plotted against average dislocation density in the deformed olivine and **b** estimated differential stress using the olivine dislocation-density piezometer. *Solid circles* and *open diamonds* represent the data obtained using a gas-medium apparatus (samples of run# 4678, 4721, 4778, 4885, 4920 from Karato et al. 1986) and a Griggs apparatus (GA210: uniaxial deformation of olivine at 1 GPa, 1,173 K, and uniaxial strain rate of $5.0 \times 10^{-5} \text{ s}^{-1}$; GA214, 223: this study), respectively. Solid line represents the best-fit defined as Eq. 1. The error in the steady-state creep strength measured by a load-cell is within 33 MPa

olivine aggregate. The strain-marker in the orthopyroxene sample rotated much more than that in the olivine sample, showing that the oriented orthopyroxene single crystal is much weaker than olivine under these conditions.

Microstructures

Typical optical photomicrographs of deformed samples are shown in Fig. 9. No subgrain formation was observed in any of the samples. The deformed samples commonly exhibit undulatory extinction. The diffraction patterns of the deformed A-orientation samples shown in Fig. 10 correspond to pure clinoenstatite, showing that the

deformation-induced phase transformation from orthoenstatite to clinoenstatite was completed. The diffraction patterns are strongly streaked parallel to a^* , resulting from the stacking faults parallel to the (100) plane. Many stacking faults (or thin lamellae) parallel to the (100) plane were observed, though no thick lamellae were observed in TEM images of the deformed A-orientation samples (Fig. 10). This suggests that the lamellae-like structures observed in optical photomicrographs (Fig. 9a, b) are caused by stacking faults. Isolated stacking faults that are ended by partial dislocations were also observed. Coe and Kirby (1975) reported that stacking faults and partial dislocations are the most prominent defects in ortho- and clinoenstatites deformed in the A-orientation geometry. Density of stacking faults in the deformed A-orientation samples decreased with the decrease in the deformation temperature.

The diffraction patterns of the deformed B-orientation samples shown in Fig. 11 correspond to pure orthoenstatite. Many dislocations are observed, though no stacking faults were observed in the deformed B-orientation samples (Fig. 11). Most of the dislocation lines are parallel to either [001] or [100] directions, suggesting that the glide plane of dislocations was (010) in the B-orientation samples (e.g., Skrotzki et al. 1990).

Flow laws

At high temperatures, plastic deformation of many materials can be described by a power-law formula, viz.,

$$\dot{\gamma} = A\tau^n \exp(-Q_d/RT) \tag{3}$$

where A is a pre-exponential constant; τ , shear stress ($= (\sigma_1 - \sigma_3)/2$); n , the stress exponent; Q_d , the apparent activation energy for dislocation creep; R , the gas constant; and T , temperature. Using the linear least-square fitting method, we obtained the flow laws for orthopyroxene deformed in the B-orientation geometry:

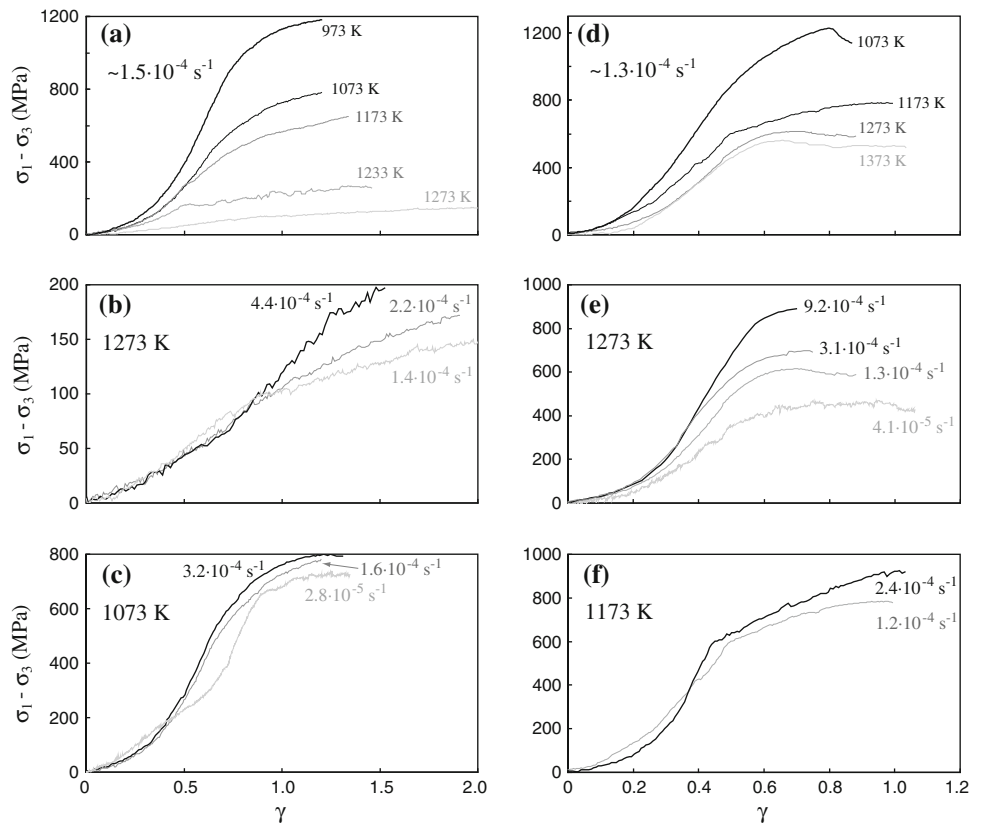
$$\dot{\gamma} = 10^{-9.5 \pm 0.1} \tau^{4.2 \pm 0.3} \exp\left(\frac{-114 \pm 18 \text{ kJ/mol}}{RT}\right) \tag{4}$$

and with the A-orientation at high temperatures ($T \geq 1,173 \text{ K}$):

$$\dot{\gamma} = 10^{8.9 \pm 0.6} \tau^{3.0 \pm 0.2} \exp\left(\frac{-459 \pm 42 \text{ kJ/mol}}{RT}\right) \tag{5}$$

When we apply the power-law formula for low-temperature data, we obtain the value of n for the A-orientation samples at low temperature ($\leq 1,173 \text{ K}$) to be 14.3. Such a high value of n is not consistent with models for power-law creep (e.g., Frost and Ashby 1982), suggesting that power-law creep is not applicable to these experimental conditions (i.e., power-law break down). At low temperatures, some mechanisms where activation

Fig. 4 Stress–strain curves for **a–c** the A-orientation and **d–f** the B-orientation samples. Dependency of the curves on temperatures and shear strain rates are summarized in **a, d** and **b, c, e, f**, respectively



enthalpy is stress dependent will operate and the flow law is expressed as follows:

$$\dot{\gamma} = B \cdot \exp \left[\frac{-Q_l (1 - \tau/\tau_p)^p}{RT} \right]^q \tag{6}$$

where B is a pre-exponential constant; Q_l , the apparent activation energy for lattice-resistance-controlled creep; τ_p , the Peierls stress; and p and q , constants ($0 < p \leq 1$; $1 < q \leq 2$) (Kocks et al. 1975). We calculated the values of B , Q_l , and τ_p using the non-linear least-square fitting method in three different cases: $(p, q) = (1, 1)$, $(1, 2)$, and $(0.5, 1.5)$ (Table 5). The best-fit curves defined as Eq. 6 are shown in Fig. 12. The following flow law for orthopyroxene deformed in the A-orientation geometry at low temperature ($T \leq 1,173$ K) is obtained:

$$\dot{\gamma} = 10^{12.6 \pm 4.3} \times \exp \left[\frac{-479 \pm 87 \text{ kJ/mol} (1 - \tau/1699 \pm 342 \text{ MPa})}{RT} \right] \tag{7a}$$

$$\dot{\gamma} = 10^{14.0 \pm 2.9} \times \exp \left[\frac{-525 \pm 98 \text{ kJ/mol} (1 - \tau/3073 \pm 546 \text{ MPa})^2}{RT} \right] \tag{7b}$$

$$\dot{\gamma} = 10^{10.7 \pm 2.3} \times \exp \left[\frac{-560 \pm 110 \text{ kJ/mol} (1 - \tau/3559 \pm 842 \text{ MPa})^{0.5}}{RT} \right]^{1.5} \tag{7c}$$

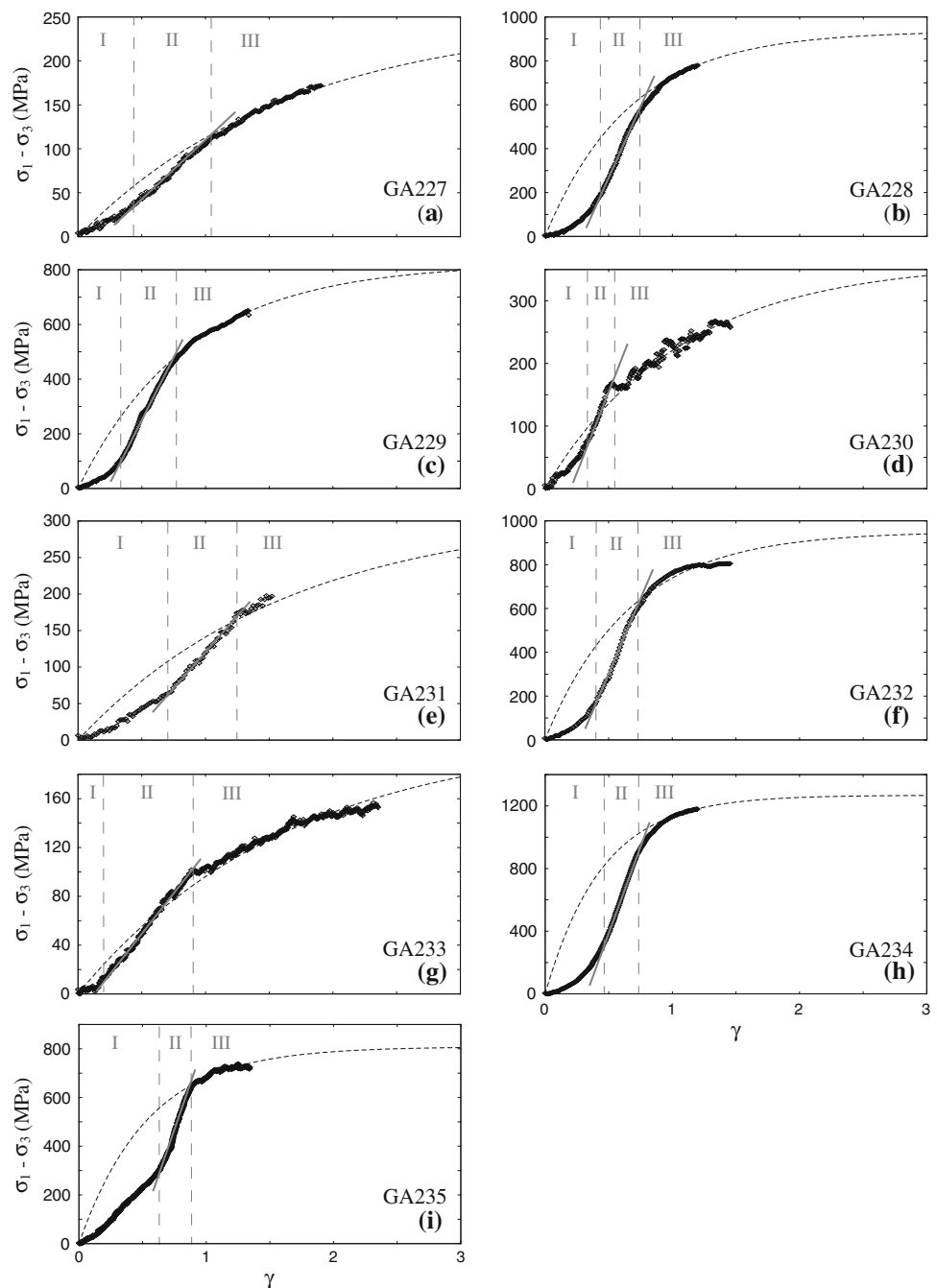
Although the creep strength data of the B-orientation samples are well described by power-law creep, the mechanical data for the B-orientation samples can also be fitted by the exponential flow law (Fig. 12). Therefore, we calculated the values of B , Q_l , and τ_p for the samples (Table 5).

Discussion

Deformation mechanisms and comparison to other experiments

Previous studies reported that the creep strength of polycrystalline orthopyroxene is controlled by slip (dislocation creep) mainly on the (100) [001] slip system and a deformation-induced phase transformation from orthoenstatite to clinoenstatite (shear on {100} in the [001] direction) at

Fig. 5 Stress–strain curves for the A-orientation samples. The curves are distributed into three regions: (I) initial period region (II) linear hardening region, and (III) parabolic hardening region. Solid lines are the best fits for the curves in the linear hardening region. Short-dashed curves are the best fits defined as Eq. 2 for the curves in the parabolic hardening region



high and low temperatures, respectively (Raleigh et al. 1971; Ross and Nielsen 1978). The boundary between the fields of two different creep mechanisms has been considered to be a function of temperature and strain rate (Raleigh et al. 1971). In the case of our experimental conditions of strain rate, the boundary is reported to be in the range of $T \sim 1,400\text{--}1,500$ K (Raleigh et al. 1971). However, it has been reported that deformation is accommodated by the phase transformation of orthoenstatite to clinoenstatite only up to $\gamma \sim 0.27$, but beyond this strain deformation is accomplished mainly by slip in

clinoenstatite (Coe and Kirby 1975). In fact, the deformed A-orientation samples are pure clinoenstatite (Fig. 10), namely the phase transformation of orthoenstatite to clinoenstatite was completed during the deformation. Figure 13 shows that the creep strength of orthopyroxene is similar to that of clinopyroxene (Kollé and Blacic 1983). Although the creep strength of clinopyroxene on the (100) [001] slip system (Kollé and Blacic 1983) is somewhat higher than that of our A-orientation samples, the presence of “kinks” on their $10,000/T - \log(\sigma_1 - \sigma_3)$ curves at $T \sim 1,173$ K (i.e., $10,000/T \sim 8.5$ K⁻¹) is a common

Table 4 Estimated values of steady-state creep strength of the A-orientation samples

Run no.	Steady-state creep strength τ_s (MPa) ^a	C ^b
GA227	250	1.3
GA228	936	3.0
GA229	823	2.3
GA230	362	1.9
GA231	312	1.3
GA232	951	2.0
GA233	212	1.2
GA234	1,268	4.0
GA235	808	3.7

^a Estimated values of steady-state creep strength of the A-orientation samples obtained by fitting the strain–stress curves in the parabolic region with Eq. 2

^b Best-fit values of the constant in Eq. 2

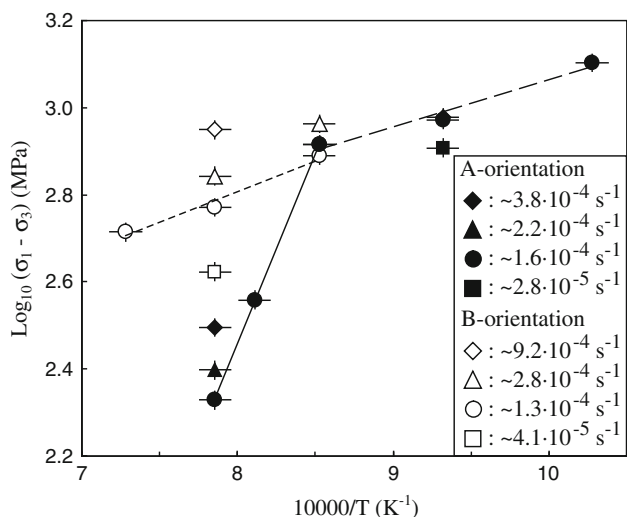


Fig. 6 Creep strength of orthopyroxene samples plotted against inverse temperatures. Solid and open symbols represent strength of the A-orientation and B-orientation samples, respectively. Long-dashed, solid, and short-dashed lines are the best fits defined as Eq. 3 for the A-orientation samples at low ($\leq 1,173$ K) and high ($\geq 1,173$ K) temperatures, and the B-orientation samples, respectively. Shear strain rates are shown with legends

feature. This suggests that the creep strength of the A-orientation samples corresponds to that of clinoenstatite after the phase transformation.

Ross and Nielsen (1978) conducted deformation experiments on polycrystalline orthopyroxene and reported that slip on the (100) [001] system was dominant at the uniaxial strains of 5–60%, and slip along the second system (010) [001] was also observed at strains $>40\%$. This is because deformation on the (100) [001] system became inoperative during extreme rotation of grains. Their observation shows

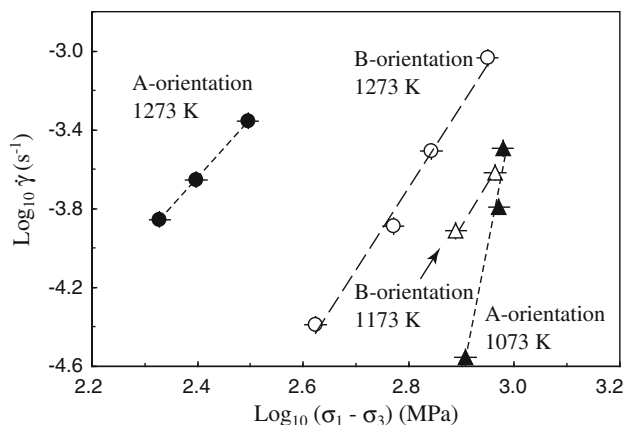


Fig. 7 Strain rate dependence of creep strength of orthopyroxene. Shear strain rates of orthopyroxene samples plotted against creep strength. Solid circles and triangles represent the strength of A-orientation samples at 1,273 and 1,073 K, respectively. Open circles and triangles represent the strength of the B-orientation samples at 1,273 and 1,173 K, respectively. The lines are the best fits defined as Eq. 3

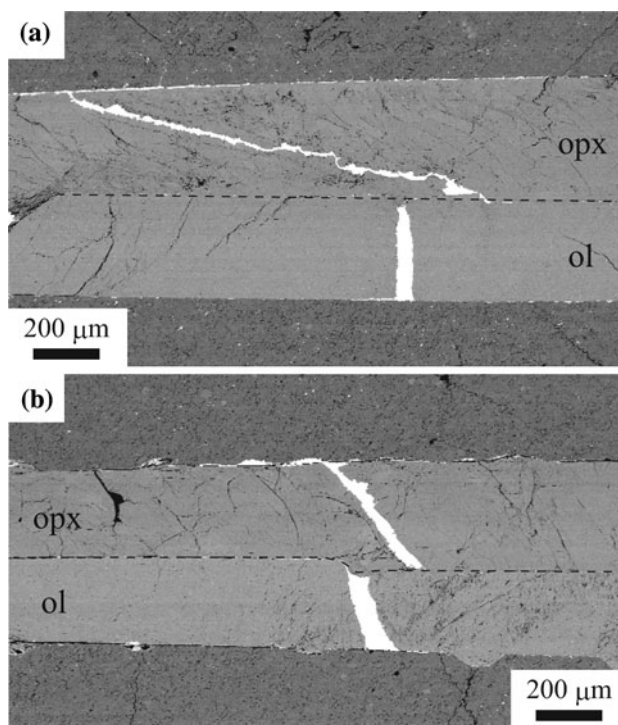


Fig. 8 Backscattered electron images of deformed A-orientation orthopyroxene (opx) and olivine (ol) samples. The samples were deformed at 1,273 K (a GA233) and 1,073 K (b GA235). The platinum strain-marker (white line in samples) was originally perpendicular to the sample plane. The rotation angle of the strain-marker in the orthopyroxene sample (75° : GA233; 44° : GA235) is much larger than that in the olivine sample ($\sim 0^\circ$: GA233; 22° : GA235). The long axes of the images are parallel to the shear direction

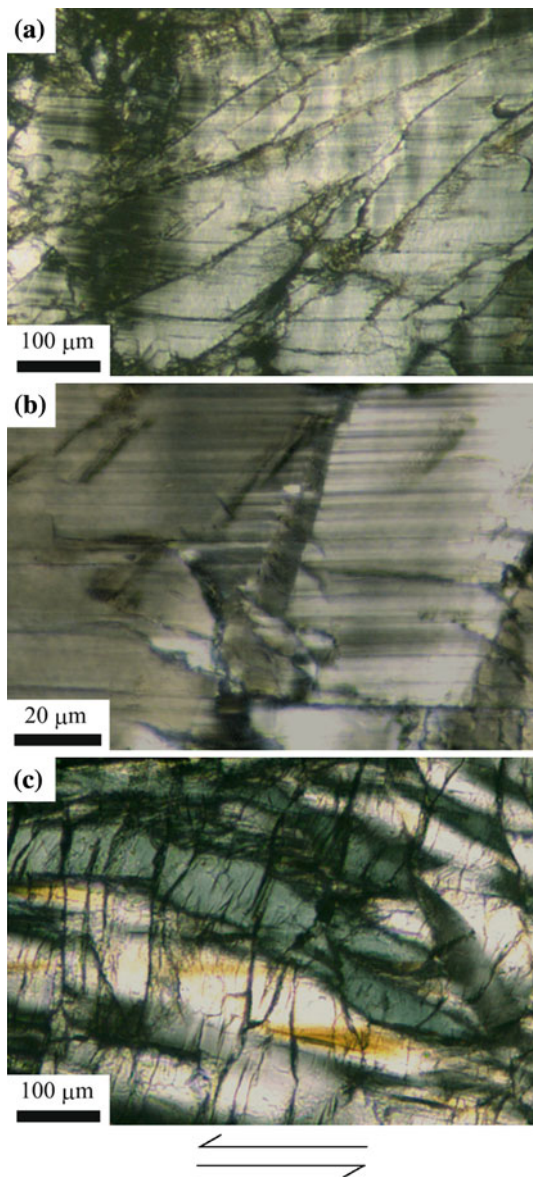


Fig. 9 Photomicrographs of deformed orthopyroxene samples in cross-polarized light. **a, b** Photomicrographs of an A-orientation sample (GA 227) parallel to the (010) plane. **c** A photomicrograph of a B-orientation sample (GA217) parallel to the (100) plane. The long axes of the photomicrographs are parallel to the shear direction ([001] direction: shown by arrows)

that the (010) [001] slip system is important as well as the (100) [001] slip system.

Figure 13 shows that the creep strength of orthopyroxene is much smaller than that of protoenstatite (Mackwell 1991) at low temperatures ($T \leq 1,373$ K). This shows that estimating the creep strength of orthopyroxene under lithospheric conditions (i.e., low- T) using the protoenstatite flow laws results in overestimation of the strength. The creep strength of orthopyroxene is smaller than that of polycrystalline olivine at low temperatures ($T \leq 1,373$ K) (Durham and Goetze 1977; Evans and Goetze 1979;

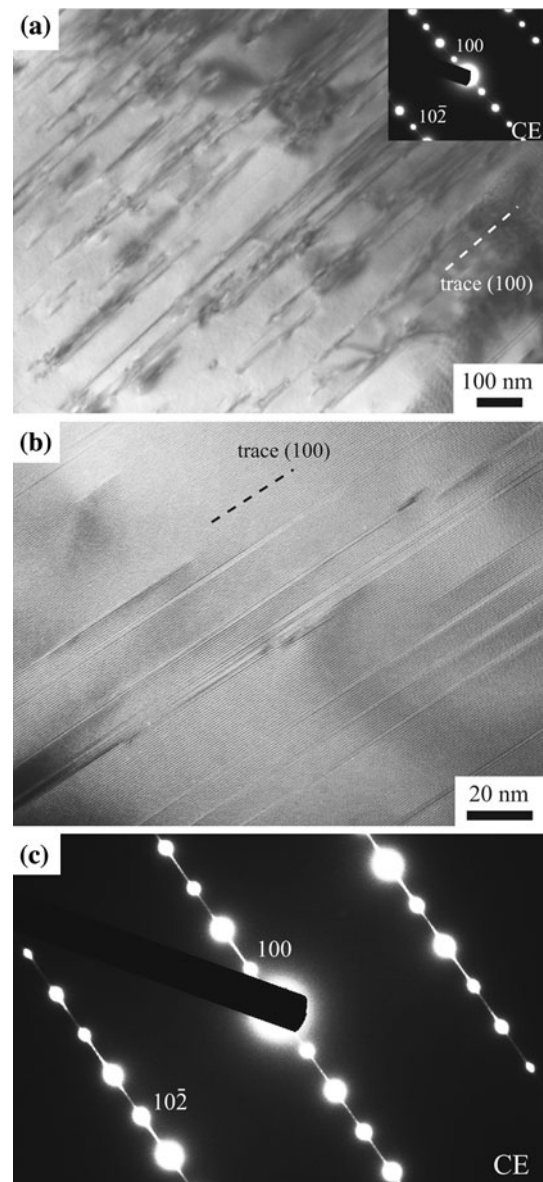


Fig. 10 Bright-field TEM images and diffraction patterns of a deformed A-orientation sample (GA227). The images were taken with **a** relatively low and **b** high magnifications. **c** The diffraction pattern of **b**. Many stacking faults parallel to the (100) plane are observed. Note that the diffraction patterns show that the deformed samples are pure clinoenstatites (CE)

Chopra and Paterson 1981; Karato et al. 1986) (Fig. 13). This is consistent with the results from orthopyroxene-olivine two-layer deformation experiments (Fig. 8). The creep strength of polycrystalline olivine is in the range of that of olivine single crystals reported by Durham and Goetze (1977) and Phakey et al. (1972) at high and low temperatures, respectively. At relatively high temperatures ($T = 1,373$ – $1,473$ K), the creep strength of olivine single crystals oriented with the $[101]_c$ direction (Demouchy et al. 2009) is significantly lower than that of polycrystalline

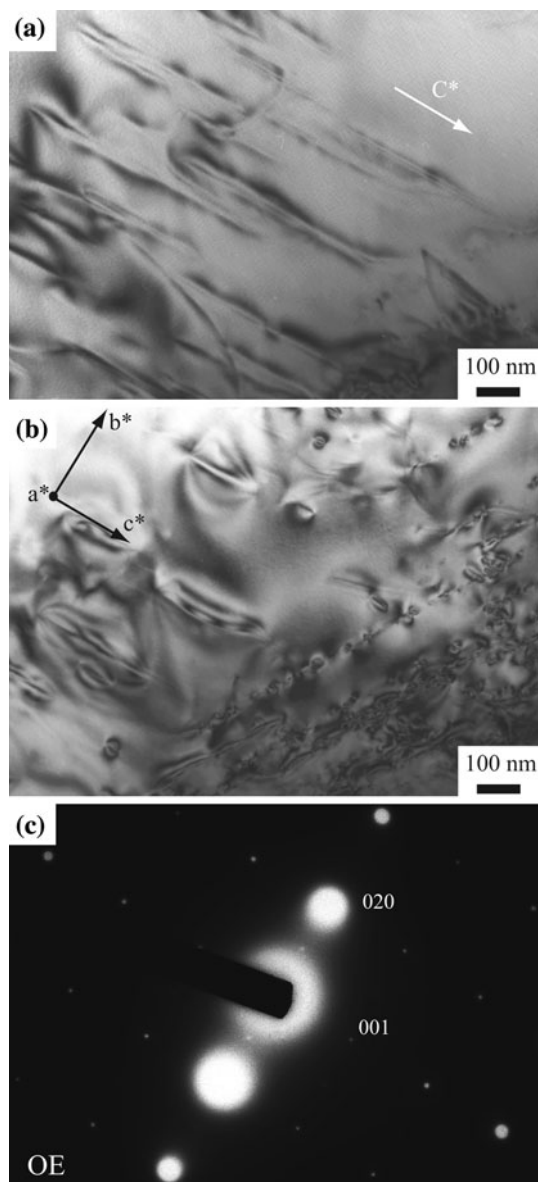


Fig. 11 Bright-field TEM images and a diffraction pattern of a deformed B-orientation sample (GA219) showing typical dislocation microstructures in the sample. **c** The diffraction pattern of both **a** and **b**. Note that the diffraction pattern shows that the deformed samples are pure orthoenstatites (OE)

olivine and similar to that of the B-orientation samples (the notation $[101]_c$ indicates a crystal compressed along a direction 45° to the $[100]$ and $[001]$ axes and 90° to the $[010]$ axis). The creep strength of the A-orientation samples is lower than that of polycrystalline olivine and olivine single crystals at a wide range of temperatures.

It has been reported that water partitioning between olivine and orthopyroxene is strongly dependent on temperature and pressure, and the water partition coefficient C_w^{opx}/C_w^{ol} (where C_w^{opx} and C_w^{ol} are the water content in orthopyroxene and olivine, respectively) is expected to be

>10 under the present experimental conditions (Keppler and Bolfan-Casanova 2006). In fact, water content in the deformed orthopyroxene samples (771–844 ppm H/Si) was 10–13 times higher than that in the deformed olivine samples (66–76 ppm H/Si) in the orthopyroxene-olivine two-layer deformation experiments (GA233, 235). High water solubility in orthopyroxene may contribute to the weakening of orthopyroxene under lithospheric conditions. Considering that the water content in the deformed olivine samples is sufficiently low (66–76 ppm H/Si), the water fugacity in the present experiments would be comparable to that in previous studies on the deformation of dry olivine.

Implications for the strength of oceanic lithosphere

Here, we will briefly discuss the possible implications of the present results on the strength of the (oceanic) lithosphere. A common problem of the strength profile, such as the one published by Kohlstedt et al. (1995), is the very high strength in the “core” region (~ 20 – 40 km from the surface) of the oceanic lithosphere approaching ~ 800 MPa. One of the reasons for such a high strength is the assumption that the strength (in the ductile regime) is controlled by that of olivine. This assumption can be challenged based on our new data on the creep strength of orthopyroxene.

Based on the flow laws for orthopyroxene obtained in this study and polycrystalline olivine (olivine lattice-resistance-controlled creep: Evans and Goetze 1979; olivine power-law creep: Chopra and Paterson 1981 and Karato et al. 1986), we calculated strength profiles for olivine and orthopyroxene under conditions for the oceanic lithosphere with a constant natural strain rate (10^{-15} /s) (Fig. 14). A geotherm for 60-m.y.-old oceanic lithosphere (Turcotte and Schubert 1982) was used for the calculation. A rheology for nearly “dry” mantle rocks was used because water is effectively removed from the rock during decompression melting in the upwelling mantle (for the water content of orthopyroxene see Table 2). Figure 14 shows that the flow of orthopyroxene in the B-orientation or the A-orientation geometry is expected to be controlled by dislocation creep at high temperatures (B-orientation: >380 K; A-orientation: >780 K). Lattice-resistance-controlled creep would control the flow of orthopyroxene at lower temperatures. Because the apparent activation energy for creep with the B-orientation is much smaller than that for the A-orientation (Table 5), the creep strength of orthopyroxene with the B-orientation is much smaller than that with the A-orientation at shallow depths (<40 km). Therefore, orthopyroxene with these orientations will be much weaker than olivine under these shallow lithosphere conditions. Although Fig. 14 suggests that the $(010)[001]$ slip system controls the strength of orthopyroxene, deformation of orthopyroxene associated with a deformation-induced

Table 5 Parameters for the flow laws

Group	Power-law creep			Creep controlled by lattice resistance			
	Log ₁₀ A (s ⁻¹ MPa ⁻ⁿ)	n	Q _d (kJ/mol)	Log ₁₀ B (s ⁻¹)	τ _p (MPa)	Q _l (kJ/mol)	
A-orientation sample (T > 1,173 K)	8.9 ± 0.6	3.0 ± 0.2	459 ± 42				
A-orientation sample (T < 1,173 K)	-27.4 ± 0.9	14.3 ± 2.5	296 ± 20	p, q = 1 p = 1, q=2 p=0.5, q=1.5	12.6 ± 4.3 14.0 ± 2.9 10.7 ± 2.3	1,699 ± 342 3,073 ± 546 3,559 ± 842	479 ± 87 525 ± 98 560 ± 110
B-orientation sample	-9.5 ± 1.0	4.2 ± 0.3	114 ± 18	p, q = 1 p = 1 > q = 2 p = 0.5, q = 1.5	0.9 ± 0.1 1.3 ± 0.6 0.7 ± 0.3	1,132 ± 241 2,048 ± 337 2,467 ± 546	160 ± 32 179 ± 15 201 ± 17

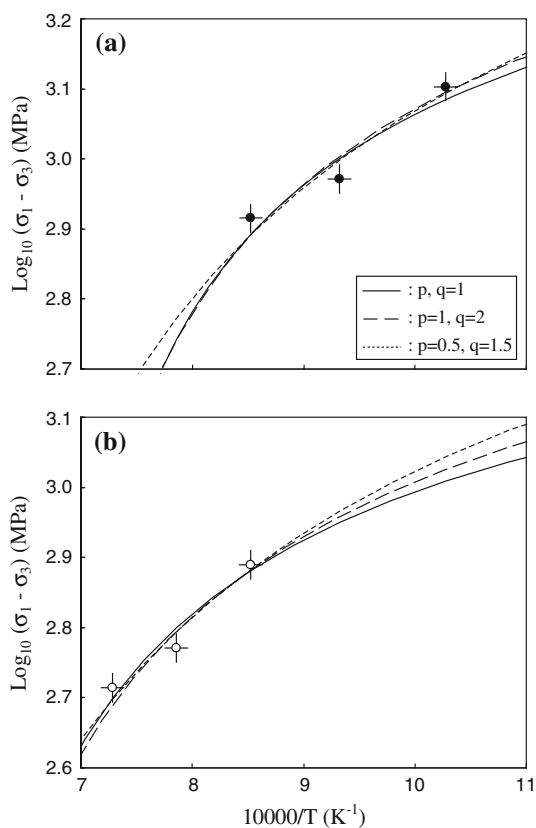


Fig. 12 Best-fit curves for the temperature dependency of creep strength of **a** the A-orientation and **b** B-orientation samples based on the flow law for creep controlled by lattice resistance to glide (Eq. 6). Solid, dashed, and dotted lines are the best fits for the case of (p, q) = (1, 1), (1, 2), and (0.5, 1.5), respectively. The symbols represent the same meanings as in Fig. 6

phase transformation (i.e., deformation of orthopyroxene with A-orientation) is also expected under low-temperature and high strain-rate conditions (Raleigh et al. 1971). In fact, Skrotzki et al. (1990) reported clinoenstatite lamellae in orthopyroxene grains in Iherzolites (Balmuccia massif, Italy), and they estimated the condition of the formation of clinoenstatite lamellae as $\sigma_1 - \sigma_3 \sim 300$ MPa and

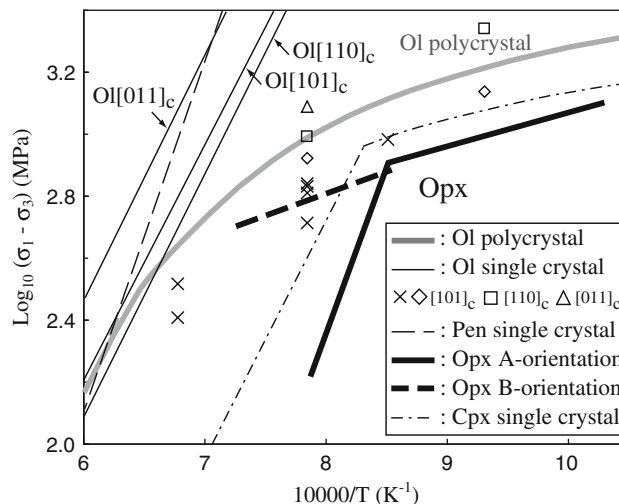


Fig. 13 Creep strength of olivine (Ol), protoenstatite (Pen), and clinopyroxene (Cpx) plotted against inverse temperatures at a constant shear strain rate of $1.3 \times 10^{-4} \text{ s}^{-1}$. The curves are calculated using the flow laws in previous studies (polycrystalline olivine power-law: Chopra and Paterson 1981; Karato et al. 1986; power-laws of olivine single crystals oriented with the [110], [110]_c, and [011]_c directions: Durham and Goetze 1977; olivine lattice-resistance-controlled creep: Evans and Goetze 1979; power-law of protoenstatite single crystal oriented with the [101]_c direction: Mackwell 1991; power-law and lattice-resistance-controlled creep of clinopyroxene single crystal on the (100) [001] slip system: Kollé and Blacic 1983). Open diamonds, squares, and triangle represent the creep strength of olivine single crystals oriented with the [101]_c, [110]_c, and [011]_c directions reported by Phakey et al. (1972). Crosses represent the creep strength of olivine single crystals oriented with the [101]_c direction reported by Demouchy et al. (2009). Note that the olivine single-crystal data were corrected to a strain rate of $1.3 \times 10^{-4} \text{ s}^{-1}$ using the value of $n = 3.5$ for olivine single crystals reported by Bai et al. (1991)

$T \sim 920$ K. Substituting these values into the flow law for the A-orientation sample (Eq. 4), the natural strain rate is estimated to be $\sim 2 \times 10^{-11} \text{ s}^{-1}$. This strain rate satisfies the conditions for the formation of clinoenstatite lamellae ($>10^{-14} \text{ s}^{-1}$ at 920 K: Raleigh et al. 1971).

The creep strength of orthopyroxene is much smaller than that of olivine although the strength of orthopyroxene

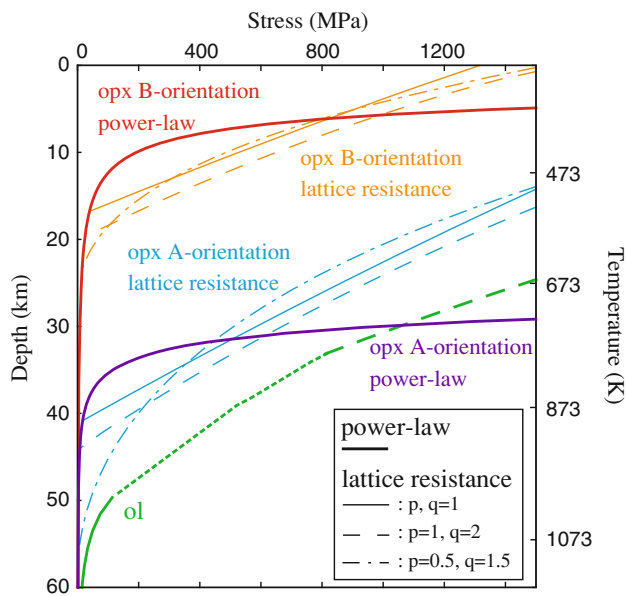


Fig. 14 Calculated creep strength of orthopyroxene (opx) deformed in the A- and B-orientation geometries and olivine polycrystalline (ol) (Evans and Goetze 1979; Chopra and Paterson 1981; Karato et al. 1986) as a function of depth in the oceanic lithosphere under a constant natural strain rate ($10^{-15}/s$). *Thick solid curves* represent the strength controlled by power-law creep. *Thin solid, dashed and dot-dashed curves* represent the strength controlled by lattice-resistance-controlled creep with $(p, q) = (1, 1)$, $(1, 2)$, and $(0.5, 1.5)$, respectively. Note that the power-law and the lattice-resistance-controlled creep for orthopyroxene deformed in each geometry are derived from the same experimental data. *Green dotted curve* represents the transition between the two different creep mechanisms of olivine

is highly anisotropic. Consequently, orthopyroxene grains oriented in favorite orientations will act as weak inclusions that will enhance deformation. If the role of weak orthopyroxene is substantial, then the strength of the lithosphere would be lower than that estimated on the basis of olivine rheology. However, there are major uncertainties in applying the present results to estimate the strength of the lithosphere. The creep strength of orthopyroxene is highly anisotropic, and therefore weak orthopyroxene will be only a small fraction of orthopyroxene grains. It is not clear how a small fraction of orthopyroxene can help reducing the overall strength of the lithosphere. It would be essential (1) to conduct large-strain deformation experiments on olivine + orthopyroxene mixtures in order to investigate the role of orthopyroxene on the strength and (2) to investigate the deformation microstructures of naturally deformed peridotites at different temperatures. There are some reports on highly elongated orthopyroxene ribbons in some peridotites deformed at relatively low temperatures (e.g., Suhr 1993). However, the significance of such unusual texture for the overall strength of the lithosphere is unknown. Also there is a well-known texture of “sheared

herzolites” from mantle xenoliths found in kimberlite magmas showing fine grained thin layers of orthopyroxene suggesting that deformation was concentrated in orthopyroxene regions (e.g., Boullier and Gueguen 1975). The combined effects of grain-size reduction and second phase (i.e., orthopyroxene) pinning during the deformation of peridotites under lithospheric conditions may cause a transition from dislocation creep to diffusion creep, resulting in weakening of the lithosphere (Warren and Hirth 2006). Again, however, the significance of these rocks on the long-term deformation of the lithosphere is not known because the estimated strain rates in these rocks are much higher than typical geological strain rates (e.g., Goetze 1975; Skemer and Karato 2008). Also, it should be emphasized that the present study was on water-poor orthopyroxene. The role of water on the creep strength and the deformation mechanisms (slip systems, etc.) needs to be investigated. Also, the processes of dynamic recrystallization and the flow law for grain-size sensitive deformation mechanisms must be investigated experimentally. Many more experimental studies and studies on naturally deformed rocks need to be conducted to understand the role of orthopyroxene in controlling the strength of the lithosphere.

Acknowledgments We thank J. Korenaga and D. Spengler for discussion and Z. Jiang for technical assistance. Official review by two anonymous reviewers improved the manuscript. This study was supported by a research fellowship from Japan Society for the Promotion of Science (to T. Ohuchi), US National Science Foundation grants (to S. Karato), and the Global COE program of Ehime University.

References

- Anastasiou P, Seifert F (1972) Solid solubility of Al_2O_3 in enstatite at high temperatures and 1–5 kb water pressure. *Contrib Mineral Petrol* 34:272–287
- Bai Q, Mackwell SJ, Kohlstedt DL (1991) High-temperature creep of olivine single crystals 1. Mechanical results for buffered samples. *J Geophys Res* 96:2441–2463
- Balachandar S, Yuen D, Reuteler D (1995) Localization of toroidal motion and shear heating in 3-d high Rayleigh number convection with temperature-dependent viscosity. *Geophys Res Lett* 22:477–480
- Bercovici D (2003) The generation of plate tectonics from mantle convection. *Earth Planet Sci Lett* 205:107–121
- Boullier AM, Gueguen Y (1975) SP-mylonites: Origin of some mylonites by superplastic flow. *Contrib Mineral Petrol* 50:93–104
- Braun J, Chery J, Poliakov A, Mainprice D, Vauchez A, Tomassi A, Daignieres M (1999) A simple parameterization of strain localization in the ductile regime due to grain size reduction: a case study for olivine. *J Geophys Res* 104:25167–25181
- Bystricky M, Mackwell S (2001) Creep of dry clinopyroxene aggregates. *J Geophys Res* 106:13443–13454
- Carter JL (1970) Mineralogy and chemistry of the Earth’s upper mantle based on the partial fusion–partial crystallization model. *Bull Geol Soc Am* 81:2021–2034

- Chopra PN, Paterson MS (1981) The experimental deformation of dunite. *Tectonophysics* 78:453–473
- Coe RS, Kirby SH (1975) The orthoenstatite to clinoenstatite transformation by shearing and reversion by annealing: mechanism and potential applications. *Contrib Mineral Petrol* 52:29–55
- Demouchy S, Schneider SE, Mackwell SJ, Zimmerman ME, Kohlstedt DL (2009) Experimental deformation of olivine single crystals at lithospheric temperatures. *Geophys Res Lett* 36:L04304. doi:10.1029/2008GL036611
- Durham WB, Goetze C (1977) Plastic flow of oriented single crystal of olivine, I, mechanical data. *J Geophys Res* 82:5737–5753
- Evans B, Goetze C (1979) The temperature variation of hardness of olivine and its implication for polycrystalline yield stress. *J Geophys Res* 84:5505–5524
- Frost HJ, Ashby MF (1982) Deformation-mechanism maps: the plasticity and creep of metals and ceramics. Pergamon, New York, 167 pp
- Gleason GC, Tullis J (1993) Improving flow laws and piezometers for quartz and feldspar aggregates. *Geophys Res Lett* 20:2111–2114
- Goetze C (1975) Sheared lherzolites: from the point of view of rock mechanics. *Geology* 3:172–173
- Hiraga T, Tachibana C, Ohashi N, Sano S (2010) Grain growth systematics for forsterite ± enstatite aggregates: effect of lithology on grain size in the upper mantle. *Earth Planet Sci Lett* 291:10–20
- Hitchings RS, Paterson MS, Bitmead J (1989) Effects of iron and magnetite additions in olivine-pyroxene rheology. *Phys Earth Planet Sci* 55:277–291
- Ingrin J, Skogby H (2000) Hydrogen in nominally anhydrous upper-mantle minerals: concentration levels and implications. *Eur J Mineral* 12:543–570
- Jung H, Karato S (2001) Effects of water on dynamically recrystallized grain-size of olivine. *J Struct Geol* 23:1337–1344
- Karato S, Jung H (2003) Effects of pressure on high-temperature dislocation creep in olivine. *Philos Mag* A83:401–414
- Karato S, Lee K-H (1999) Stress and strain distribution in deformed olivine aggregates: inference from microstructural observations and implications for texture development. In: Szpunar JA (ed) Proceedings of the twelfth international conference on textures of materials, ITOCOM-12, vol 2. pp 1546–1555
- Karato S, Paterson MS, Fitz Gerald JD (1986) Rheology of synthetic olivine aggregates: influence of water and grain size. *J Geophys Res* 91:8151–8176
- Karato S, Jung H, Katayama I, Skemer P (2008) Geodynamic significance of seismic anisotropy of the upper mantle: new insights from laboratory studies. *Annu Rev Earth Planet Sci* 36:59–95
- Kepler H, Bolfan-Casanova N (2006) Thermodynamics of water solubility and partitioning. *Rev Mineral Geochem* 62:193–230
- Kocks WF, Argon AS, Ashby MF (1975) Thermodynamics and kinetics of slip. *Prog Mater Sci* 19:1–291
- Kohlstedt DL, Goetze C, Durham WB (1976) Experimental deformation of single crystal olivine with application to flow in the mantle. In: Strens RGJ (ed) The physics and chemistry of minerals and rocks. Wiley, New York, pp 35–49
- Kohlstedt DL, Nichols HPK, Hornack P (1980) The effect of pressure on the rate of dislocation recovery in olivine. *J Geophys Res* 88:3122–3130
- Kohlstedt DL, Evans B, Mackwell S (1995) Strength of the lithosphere: constraints imposed by laboratory experiments. *J Geophys Res* 100:17587–17602
- Kollé JJ, Blacic JD (1983) Deformation of single-crystal clinopyroxenes: 2. Dislocation-controlled flow processes in hedenbergite. *J Geophys Res* 88:2381–2393
- Korenaga J (2007) Thermal cracking and the deep hydration of oceanic lithosphere: a key to the generation of plate tectonics? *J Geophys Res* 112:B05408. doi:10.1029/2006JB004502
- Mackwell SJ (1991) High-temperature rheology of enstatite: implications for creep in the mantle. *Geophys Res Lett* 18:2027–2030
- Mirwald PW, Getting IC, Kennedy GC (1975) Low-friction cell for piston-cylinder high-pressure apparatus. *J Geophys Res* 80:1519–1525
- Mitchell TE, Thornton PR (1963) Work-hardening characteristics of Cu and alpha-brass single crystals between 4.2 and 500 degrees K. *Philos Mag* 8:1127–1159
- Ohuchi T, Nakamura M (2007) Grain growth in the forsterite–diopside system. *Phys Earth Planet Inter* 160:1–21
- Paterson MS (1982) The determination of hydroxyl by infrared absorption in quartz, silicate glasses and similar materials. *Bull Minéral* 105:20–29
- Phakey P, Dollinger G, Christie J (1972) Transmission electron microscopy of experimentally deformed olivine crystals. In: Heard HC et al (eds) Flow and fracture of rocks: the Griggs volume, Geophysical Monograph Series, vol 16. AGU, Washington, DC, pp 117–138
- Raleigh CB, Kirby SH, Carter NL, Ave' Lallemand HG (1971) Slip and the clinoenstatite transformation as competing rate processes in enstatite. *J Geophys Res* 76:4011–4022
- Richards MA, Yang W-S, Baumgardner JR, Bunge H-P (2001) Role of a low-viscosity zone in stabilizing plate tectonics: Implications for comparative terrestrial planetology. *Geochem Geophys Geosyst* 2. doi:10.1029/2000GC000115
- Ross JV, Nielsen KC (1978) High-temperature flow of wet polycrystalline enstatite. *Tectonophysics* 44:233–261
- Rybacki E, Renner J, Konrad K, Harbott W, Rummel F, Stöckhert B (1998) A servohydraulically-controlled deformation apparatus for rock deformation under conditions of ultra-high pressure metamorphism. *Pure Appl Geophys* 152:579–606
- Seeger A (1957) Dislocations and mechanical properties of crystals (ed. Fisher JC), 243 pp. Wiley, New York
- Skemer P, Karato S (2008) Sheared lherzolite xenoliths revisited. *J Geophys Res* 113:B07205. doi:10.1029/2007JB005286
- Skrotzki W, Wedel A, Weber K, Müller WF (1990) Microstructure and texture in lherzolites of the Balmuccia massif and their significance regarding the thermomechanical history. *Tectonophysics* 179:227–251
- Smith BK, Carpenter FO (1987) Transient creep in orthosilicates. *Phys Earth Planet Sci* 49:314–324
- Solomatov VS, Moresi L (1997) Stagnant lid convection on venus. *J Geophys Res* 101:4737–4753
- Suhr G (1993) Evaluation of upper mantle microstructures in the Table Mountain massif (Bay of Islands ophiolite). *J Struct Geol* 15:1273–1292
- Tackley PJ (2000) Self-consistent generation of tectonic plates in time-dependent, three-dimensional mantle convection simulations 2. Strain weakening and asthenosphere. *Geochem Geophys Geosyst* 1. doi:10.1029/2000GC000043
- Turcotte DL, Schubert G (1982) Geodynamics: applications of continuum physics to geological problems, 450 pp. Wiley, New York
- Warren JM, Hirth G (2006) Grain size sensitive deformation mechanisms in naturally deformed peridotites. *Earth Planet Sci Lett* 248:438–450
- Zhang J, Green HW (2007) Experimental investigation of eclogite rheology and its fabrics at high temperature and pressure. *J Metamorphic Geol* 25:97–115